The Astrophysical Journal Supplement Series, 274:42 (10pp), 2024 October https://doi.org/10.3847/1538-4365/ad7d01

High-quality Extragalactic Legacy-field Monitoring (HELM) with DECam: Project Overview and First Data Release

Ming-Yang Zhuang (庄明阳)[1], Qian Yang[1,2], Yue Shen[1,3], Monika Adamów[4], Douglas N. Friedel[3], R. A. Gruendl[3], Zachary Stone[1,4], Junyao Li[1], Xin Liu[1,3,5], Paul Martini[6,7], Timothy M. C. Abbott[8], Scott F. Anderson[9], Roberto J. Assef[10], Franz E. Bauer[11,12,13], Richard Bielby[14], W. N. Brandt[15,16,17], Colin J. Burke[1], Jorge Casares[18,19], Yu-Ching Chen[1], Gisella De Rosa[20], Alex Drlica-Wagner[21,22,23], Tom Dwelly[24], Alice Eltvedt[14], Gloria Fonseca Alvarez[25], Jianyang Fu (傅健洋)[1], Cesar Fuentes[13,26,27], Melissa L. Graham[28], Catherine J. Grier[29,30], Nathan Golovich[31], Patrick B. Hall[32], Patrick Hartigan[33], Keith Horne[34], Anton M. Koekemoer[20], Mirko Krumpe[35], Jennifer I. Li[36], Chris Lidman[37,38], Umang Malik[37], Amelia Mangian[39], Andrea Merloni[24], Claudio Ricci[40,41], Mara Salvato[24], Rob Sharp[37], David E. Trilling[42], Brad E. Tucker[37,43,44], Di Wen[1], Zachary Wideman[45], Yongquan Xue[46], Zhefu Yu[47], and Catherine Zucker[2]

[1] Department of Astronomy, University of Illinois Urbana-Champaign, Urbana, IL 61801, USA; mingyang@illinois.edu
[2] Center for Astrophysics | Harvard & Smithsonian, 60 Garden Street, Cambridge, MA 02138, USA
[3] National Center for Supercomputing Applications, University of Illinois Urbana-Champaign, Urbana, IL 61801, USA
[4] Center for AstroPhysical Surveys, National Center for Supercomputing Applications, University of Illinois Urbana-Champaign, Urbana, IL 61801, USA
[5] Center for Artificial Intelligence Innovation, University of Illinois at Urbana-Champaign, 1205 West Clark Street, Urbana, IL 61801, USA
[6] Department of Astronomy, The Ohio State University, Columbus, OH 43210, USA
[7] Center of Cosmology and Astro-Particle Physics, The Ohio State University, Columbus, OH 43210, USA
[8] CTIO, NSF's NOIRLab, Casilla 603, La Serena, Chile
[9] Astronomy Department, University of Washington, Box 351580, Seattle, WA 98195, USA
[10] Instituto de Estudios Astrofísicos, Facultad de Ingeniería y Ciencias, Universidad Diego Portales, Av. Ejército Libertador 441, Santiago, Chile
[11] Instituto de Astrofísica, Facultad de Física, Pontificia Universidad Católica de Chile, Campus San Joaquín, Av. Vicuña Mackenna 4860, Macul Santiago, 7820436, Chile
[12] Centro de Astroingeniería, Facultad de Física, Pontificia Universidad Católica de Chile, Campus San Joaquín, Av. Vicuña Mackenna 4860, Macul Santiago, 7820436, Chile
[13] Millennium Institute of Astrophysics, Nuncio Monseñor Sótero Sanz 100, Of 104, Providencia, Santiago, Chile
[14] Centre for Extragalactic Astronomy, Department of Physics, Durham University, South Road, Durham, DH1 3LE, UK
[15] Department of Astronomy & Astrophysics, 525 Davey Lab, The Pennsylvania State University, University Park, PA 16802, USA
[16] Institute for Gravitation and the Cosmos, The Pennsylvania State University, University Park, PA 16802, USA
[17] Department of Physics, 104 Davey Laboratory, The Pennsylvania State University, University Park, PA 16802, USA
[18] Instituto de Astrofísica de Canarias, E-38205 La Laguna, Tenerife, Spain
[19] Departamento de Astrofísica, Universidad de La Laguna, E-38206 La Laguna, Tenerife, Spain
[20] Space Telescope Science Institute, 3700 San Martin Drive, Baltimore, MD 21218, USA
[21] Fermi National Accelerator Laboratory, P.O. Box 500, Batavia, IL 60510, USA
[22] Kavli Institute for Cosmological Physics, University of Chicago, Chicago, IL 60637, USA
[23] Department of Astronomy and Astrophysics, University of Chicago, Chicago, IL 60637, USA
[24] Max-Planck Institute for Extraterrestrial Physics, Giessenbachstrasse 1, Garching, 85748, Germany
[25] NSF's NOIRLab, 950 N. Cherry Avenue, Tucson, AZ 85719, USA
[26] Departamento de Astronomía, Universidad de Chile, Camino del Observatorio 1515, Las Condes, Santiago, Chile
[27] Centro de Excelencia en Astrofísica y Tecnologías Afines (CATA), Chile
[28] DIRAC Institute, Department of Astronomy, University of Washington, 3910 15th Avenue NE, Seattle, WA 98195, USA
[29] Department of Astronomy, University of Wisconsin-Madison, Madison, WI 53706, USA
[30] Steward Observatory, The University of Arizona, 933 N. Cherry Avenue, Tucson, AZ 85721, USA
[31] Lawrence Livermore National Laboratory, 7000 E. Avenue, Livermore, CA 94550, USA
[32] Department of Physics & Astronomy, York University, 4700 Keele Street, Toronto, ON M3J 1P3, Canada
[33] Department of Physics and Astronomy, Rice University, 6100 S. Main Street, TX 77005-1892, USA
[34] University of St Andrews, SUPA School of Physics & Astronomy, North Haugh, St Andrews KY16 9SS, UK
[35] Leibniz Institute for Astrophysics Potsdam (AIP), An der Sternwarte 16, 14482 Potsdam, Germany
[36] Department of Astronomy, University of Michigan, Ann Arbor, MI 48109, USA
[37] Research School of Astronomy and Astrophysics, Australian National University, Canberra, ACT 2611, Australia
[38] Centre for Gravitational Astrophysics, College of Science, The Australian National University, Canberra ACT 2601, Australia
[39] Information Trust Institute, University of Illinois Urbana-Champaign, Urbana, IL 61801, USA
[40] Núcleo de Astronomía de la Facultad de Ingeniería, Universidad Diego Portales, Av. Ejército Libertador 441, Santiago, Chile
[41] Kavli Institute for Astronomy and Astrophysics, Peking University, Beijing 100871, People's Republic of China
[42] Department of Astronomy and Planetary Science, Northern Arizona University, Flagstaff, AZ 86011, USA
[43] National Centre for the Public Awareness of Science, Australian National University, Canberra, ACT 2601, Australia
[44] The Australian Research Council Centre of Excellence for All-Sky Astrophysics in 3 Dimension (ASTRO 3D), Australia
[45] Department of Physics and Astronomy, Texas A&M University, 4242 TAMU, College Station, TX 77843, USA
[46] CAS Key Laboratory for Research in Galaxies and Cosmology, Department of Astronomy, University of Science and Technology of China, Hefei 230026, People's Republic of China
[47] Kavli Institute for Particle Astrophysics and Cosmology, Stanford University, 452 Lomita Mall, Stanford, CA 94305, USA
Received 2024 February 8; revised 2024 September 2; accepted 2024 September 17; published 2024 October 11

Abstract

High-quality Extragalactic Legacy-field Monitoring (HELM) is a long-term observing program that photometrically monitors several well-studied extragalactic legacy fields with the Dark Energy Camera (DECam) imager on the CTIO 4 m Blanco telescope. Since 2019 February, HELM has been monitoring regions within COSMOS, XMM-LSS, CDF-S, S-CVZ, ELAIS-S1, and SDSS Stripe 82 with few-day cadences in the (u)gri(z) bands, over a collective sky area of $\sim$38 deg^2. The main science goal of HELM is to provide high-quality optical light curves for a large sample of active galactic nuclei (AGNs), and to build decades-long time baselines when combining past and future optical light curves in these legacy fields. These optical images and light curves will facilitate the measurements of AGN reverberation mapping lags, as well as studies of AGN variability and its dependencies on accretion properties. In addition, the time-resolved and coadded DECam photometry will enable a broad range of science applications from galaxy evolution to time-domain science. We describe the design and implementation of the program and present the first data release that includes source catalogs and the first $\sim$3.5 yr of light curves during 2019A–2022A.

Unified Astronomy Thesaurus concepts: Surveys (1671); Quasars (1319); Optical astronomy (1776); Time domain astronomy (2109); Galactic and extragalactic astronomy (563)

1. Introduction

Large-scale optical time-domain imaging surveys such as Sloan Digital Sky Survey (SDSS; York et al. 2000) supernova survey (M. Sako et al. 2018), Pan-STARRS1 Medium Deep Survey (K. C. Chambers et al. 2016; D. O. Jones et al. 2017), Zwicky Transient Facility (ZTF; E. C. Bellm et al. 2019), and Wide Field Survey Telescope (T. Wang et al. 2023) are rapidly shaping our understanding of the dynamic and variable Universe. In addition to transients and explosive events from stellar systems, these time-domain surveys provide extremely valuable information to probe the physical mechanisms that drive the persistent variability from variable stars and active galactic nuclei (AGNs). Variability studies of AGNs also enable the measurements of their black hole masses via the reverberation mapping (RM) technique that measures the time lag between the driving continuum variability and the delayed response in the broad-line emission (e.g., R. D. Blandford & C. F. McKee 1982; B. M. Peterson 1993). In particular, high-quality photometric light curves with long time baselines and adequate cadences are necessary to secure an RM lag measurement and periodicity searches for binary supermassive black hole candidates when combined with dedicated spectroscopic monitoring data (e.g., M. J. Graham et al. 2015; Y. Shen et al. 2015).

The SDSS-V Black Hole Mapper (BHM) program (J. A. Kollmeier et al. 2017) is conducting a multiyear (2020–2027), multiobject spectroscopic RM campaign (BHM-RM) in several legacy extragalactic fields. In order to provide the required photometric light curves that sample the AGN continuum variability, we are conducting a long-term photometric monitoring campaign with the Dark Energy Camera (DECam; B. Flaugher et al. 2015) on the 4 m CTIO Blanco telescope. The fields chosen by the SDSS-V BHM-RM program coincide with several well-studied extragalactic fields, each with ample multiwavelength data and/or earlier and future photometric light curves therein (e.g., M. Lacy et al. 2021; F. Zou et al. 2022). For example, most of these fields coincide with deep monitoring fields in the Pan-STARRS1 survey (K. C. Chambers et al. 2016) and the Dark Energy Survey supernovae program (T. M. C. Abbott et al. 2021). The combined optical light curves for most of these monitoring fields will span more than 25 yr once combined with 10 yr light curves from the Legacy Survey of Space and Time (LSST) with the Vera C. Rubin Observatory. Therefore these DECam monitoring data will provide legacy value for broad science in these fields.

In this paper we provide an overview of the DECam monitoring program and its current status, and present the first data release[48] from the first $\sim$3.5 yr of observations (2019–2022). In Section 2 we provide a technical overview of the High-quality Extragalactic Legacy-field Monitoring (HELM) program. In Section 3 we describe the data products, with examples to showcase the science applications. We summarize and provide an outlook in Section 4. We adopt AB magnitude system throughout the paper.

2. Observations and Data Processing

HELM started observations in the 2019A semester (2019 February–July) and is currently ongoing. During the early phase of the program (2019A–2020B), a cadence of $\sim$6 days was adopted. Since 2021A, the cadence was increased to $\sim$3 days and a new field (South Continuous Viewing Zone; S-CVZ) was added to the field list. For each epoch, a set of consecutive exposures in the gri bands are taken, with two back-to-back exposures for each band. The nominal per-epoch exposure times are 160, 140, and 180 s in the three bands, respectively. A total of 14 DECam pointings (each with a 2.7 deg^2 field of view) received regular monitoring, most of which are for the BHM-RM program. However, some pointings are included in different programs (PIs: X. Liu, P. Martini) that have slightly different science goals, including periodicity searches of binary supermassive black hole candidates and RM lag measurement. We consolidated these different DECam monitoring programs with AGN science focuses and processed these data with the same pipeline. Table 1 summarizes the details of the monitoring fields. Three fields (CDF-S, XMM-LSS, and COSMOS) contain three pointings, while two fields (ELAIS-S1 and SDSS Stripe 82) contain two pointings. The layouts of the HELM fields are shown in Figure 1. These particular pointings are aligned with past monitoring within the DES supernovae program (e.g., J. P. Bernstein et al. 2012; M. Smith et al. 2020).

The first two semesters of HELM (2019A–2019B) were carried out on shared nights with other nonmonitoring DECam programs. Since 2020A, HELM has been part of a collection of regular DECam monitoring programs that pool observing time

[48] https://ariel.astro.illinois.edu/helm/

Table 1
HELM Observation Summary

Field (1)	Pointing (2)	Pointing Center (3)	ProgID (4)	Filter (5)	N_{exp} (6)	5σ Depth (mag) (7)
CDF-S	C1	$03^h37^m06^s$ $-27^d06^m43^s$	C	*griz*	54-36-36-18	22.9-23.3-23.1-22.6
	C2	$03^h37^m06^s$ $-29^d05^m18^s$	A-C	*griz*	54-36-36-18	
	C3	$03^h30^m36^s$ $-28^d06^m01^s$	A-C	*griz*	248-190-187-34	
COSMOS	CO1	$10^h00^m00^s$ $+03^d05^m56^s$	A-C-E-F-G	*gri*	362-295-295	22.8-23.1-22.9
	CO2	$09^h56^m53^s$ $+01^d44^m58^s$	A-E-F-G	*gri*	278-232-235	
	CO3	$10^h03^m07^s$ $+01^d44^m59^s$	A-E-F-G	*gri*	267-226-232	
ELAIS-S1	E1	$00^h31^m30^s$ $-43^d00^m35^s$	A-C-E-F-G	*griz*	387-340-349-28	22.8-23.2-23.1-22.5
	E2	$00^h38^m00^s$ $-43^d59^m53^s$	A-C-E-F-G	*griz*	365-332-322-302	
S-CVZ	S-CVZ	$06^h00^m00^s$ $-66^d33^m39^s$	A-C	*ugriz*	33-223-196-196-24	21.1-22.8-22.9-22.7-22.0
Stripe 82	S1	$02^h51^m17^s$ $-00^d00^m03^s$	A-B-C-H	*griz*	87-50-47-16	22.7-23.5-23.4-22.8
	S2	$02^h44^m47^s$ $-00^d59^m20^s$	A-B-C-H	*griz*	82-47-47-17	
XMM-LSS	X1	$02^h17^m54^s$ $-04^d55^m48^s$	A-C	*griz*	127-107-102-20	22.6-22.9-22.7-22.4
	X2	$02^h22^m40^s$ $-06^d24^m46^s$	A-C	*griz*	127-107-102-20	
	X3	$02^h25^m48^s$ $-04^d36^m04^s$	A-C	*griz*	127-107-102-20	

Note. Column (1): field name. Column (2): pointing name. Column (3): Median coordinate of pointing center. Typical pointing accuracy of each exposure is $\sim 10''$. Column (4) Program ID. A: 2019A-0065; B: 2019B-0219; C: 2019B-0910; D: 2021A-0037; E: 2021A-0113; F: 2021B-0149; G: 2022A-724693; H: 2022B-175073. Column (5): filter used. Column (6): Number of successfully reduced exposures in each band, separated by dashes. Most of the nightly epochs in the HELM program consist of two back-to-back exposures per pointing per filter. Column (7): median 5σ depth of individual exposures for all pointings of a given field estimated from m_{PSF}.

and observers. In a few subsequent semesters, to improve the overall observing efficiency, some pointings of HELM were observed under the public DECam monitoring program that also targeted the COSMOS and ELAIS-S1 fields (M. L. Graham et al. 2023), but to greater depths than those of the HELM program. These public DECam data are included in our data reduction and data products. The monitoring program suffered significant time loss in 2020A due to the COVID-19 pandemic, and substantial loss in the second half of 2020B due to DECam instrumental problems.

At the beginning of the program during 2019A, we observed some fields with additional filters to provide more wavelength coverage. The S-CVZ field was observed in the *ugriz* filters. For these additional imaging, *griz* has 61 available CCD chips (except CCD #61), while *u* has 60 chips with an additional CCD #2 not available. Table 1 summarizes the HELM observations including fields, pointings, observing program IDs, filters, and numbers of exposures up to 2022 September 13. Figure 2 illustrates the cadence of each field.

2.1. Data Reduction

The raw HELM observations were processed using the Dark Energy Survey (DES) "Final Cut" pipeline (see E. Morganson et al. 2018 for an overview) with the same configurations of `SExtractor` (E. Bertin & S. Arnouts 1996) and `PSFEx` (E. Bertin 2011) as that used in the production campaigns for the second data release (DR2) of DES (DES-DR2; T. M. C. Abbott et al. 2021) and DECam Local Volume Exploration DR2 (A. Drlica-Wagner et al. 2022). To summarize, a set of generic corrections including crosstalk correction, bias subtraction, bad pixel masking, correcting nonlinear pixel response, and flat-fielding are first applied to all raw DECam exposures before image-specific processing. The "Final Cut" pipeline is then applied to preprocessed images, which includes initial astrometry solution calculation, saturated pixels and associated bleed trails masking, sky background subtraction, star flat correction, cosmic-ray and satellite masking, point-spread function (PSF) modeling, single-epoch catalog construction, and image data quality evaluation. `SExtractor` and `PSFEx` configurations are shown in Tables 12–14 in E. Morganson et al. (2018). A set of magnitude (flux) measurements are reported for each source in the final catalog, including PSF magnitude (measured by fitting the PSF model constructed from `PSFEx`), 12 circular aperture magnitudes, and Kron-like automatic aperture (AUTO) magnitude. During the years that the DES Collaboration was actively taking data, the calibration products (e.g., bias, flat, sky-subtraction templates, secondary flat-field or "star-flats," and the relative astrometric offsets among the CCDs) were monitored and updated as needed as part of that program. Processing of observations taken after the DES observations ended in 2019 January have, thus far, relied on the DES legacy calibration products from that period. In Section 2.2 we assess the overall systematic astrometric and photometric performance to understand the limitations this might have on the temporal monitoring by HELM.

2.1.1. Magnitude Zero-point

A magnitude zero-point (zp) pipeline is run separately for all of the CCD images. We use the `expCalib` (S. Allam & R. Gruendl, private communication) code to match objects in the Final Cut catalogs to the APASS 9 catalog (A. A. Henden et al. 2015). A $1''$ radius match was performed for each CCD in one exposure. If the number of matched objects is low or a match was not found, the average zp value among all CCDs is adopted. The expCalib will not return a match (or will return a low number of matches) in two cases: the APASS catalog has no coverage in the requested region of the sky, or the magnitude range of stars in the APASS catalog does not overlap with the brightness of objects detected in the CCD (APASS sources are brighter and appear saturated in the DECam data). Among 7816 successfully reduced exposures (corresponding to 476,743 CCD individual images), magnitude zps are available from the expCalib for all but 124 exposures

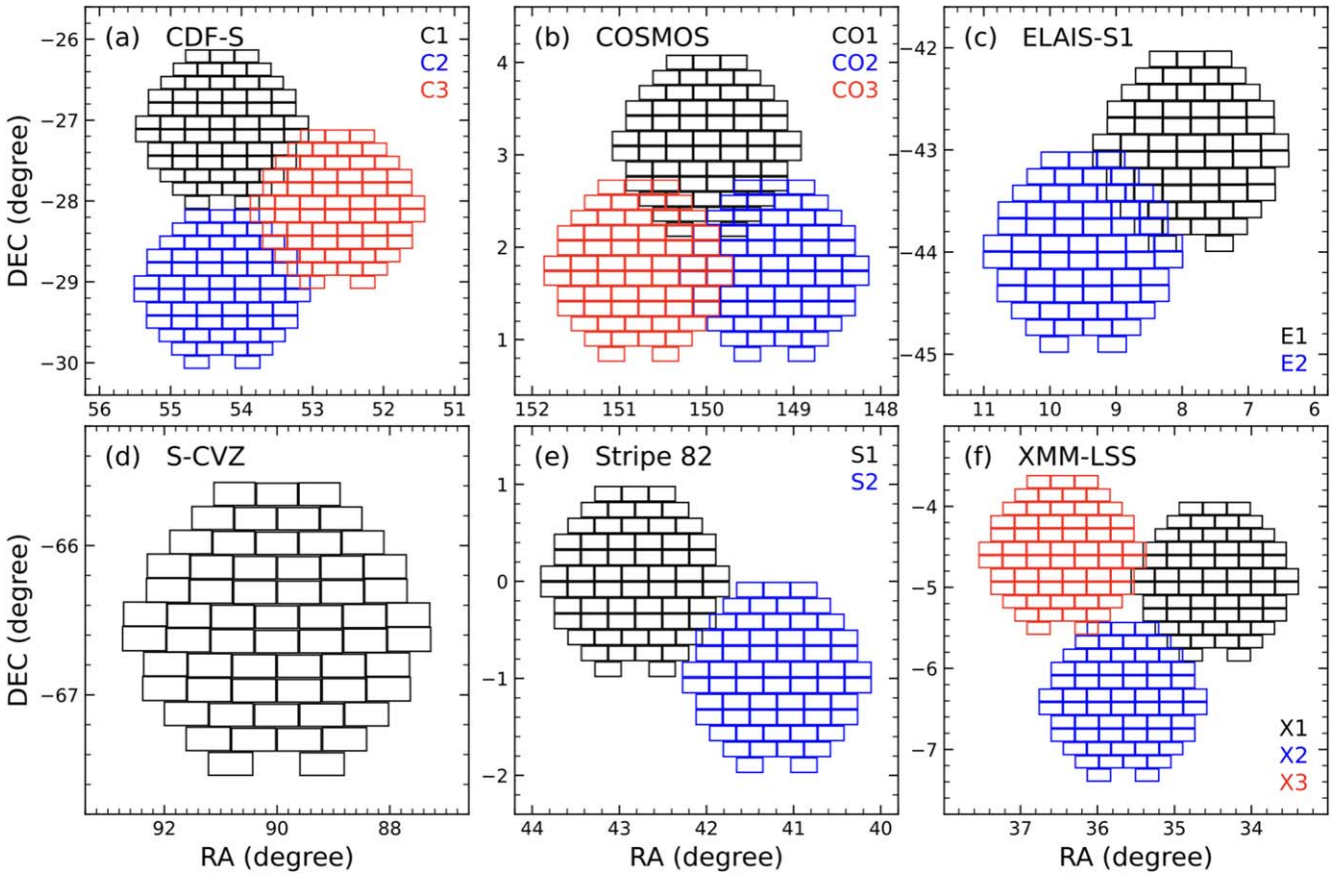

Figure 1. The layout of HELM pointings in (a) CDF-S, (b) COSMOS, (c) ELAIS-S1, (d) S-CVZ, (e) SDSS Stripe 82, and (f) XMM-LSS fields. Pointings 1, 2, and 3 are indicated in black, blue, and red colors, respectively.

(2, 49, 28, 44, and 1 in the *ugriz* bands, respectively) and 7562 CCD images (1.6%).

Using four fields associated with 10 pointings of our HELM DECam monitoring program (CDF-S, ELAIS-S1, SDSS Stripe 82, and XMM-LSS) that are covered by the footprint of 6 yr of DES science operations of $\sim$5000 deg^2 from DES-DR2 (T. M. C. Abbott et al. 2021), we derive independent magnitude zps for all exposures by crossmatching sources detected in our observations with those from the DES-DR2 source catalog. The DES-DR2 catalog is constructed using coadded images, which has typically $\sim$10 times longer exposure time than our single-exposure images. Based on the extent of the source, we derive two versions of magnitude zps, one based on point sources using $m_{\rm PSF}$ and another based on all the sources using $m_{\rm AUTO}$ to increase the number of available objects. We first select all the reliably extracted (`IMAFLAG_ISO=0`, `FLAGS` <4), high signal-to-noise ratio (SNR; $m_{\rm PSF}$ error <0.1 mag, which corresponds to an SNR of 10) sources from our observations. We use a relatively loose criterion of `CLASS_STAR` >0.8 to select pointlike sources, which ensures we do not miss a significant number of point sources and avoids including many extended sources. For the DES-DR2 catalog, we apply the same selection criteria of object quality (`IMAFLAGS_ISO=0`, `FLAGS` <4 in i band) and select pointlike sources using $0 \leqslant$ `EXTENDED_COADD` $\leqslant 1$ following T. M. C. Abbott et al. (2021).

The magnitude zp of each CCD chip is derived using the 3σ clipped median difference between magnitudes of objects from our single-exposure catalog and those from the DES-DR2 catalog, with associated error equal to the standard deviation divided by the root of the number of the remaining objects. Figure 3 compares the number of objects used to derive the magnitude zps. Magnitude zps derived from all sources make use of on average 2.7 times more objects compared to those derived from point sources only (295 versus 108). When limited to CCD images with at least 10 applicable objects for zp calibration, we find a small difference of 0.009 mag with the 16th and 84th percentiles of the distribution of -0.008 and 0.019 mag between the two sets of zps, respectively (Figure 4). We find that the difference between two zps is correlated with seeing, with larger $m_{\rm PSF}$-based zps in exposures with better seeing. This may be related to slight difference in aperture loss at different seeing conditions. We also compare the zp from the DECam pipeline with that from DES-DR2 using all sources (Table 2). The median differences are <0.01 mag (slightly larger with 0.014 mag in the E2 field) with a scatter of $\lesssim$0.04 mag. The final zp of a CCD image is determined with the priority decreasing from DES-DR2 AUTO magnitude to DES-DR2 PSF magnitude to DECam pipeline. We only adopt a DES-DR2-based zp if the number of objects used to calibrate the zp is greater or equal to 10. Finally, we successfully obtain zps for 99.9% of the CCD images, with DES-DR2 AUTO contributing to the vast majority of them (99.4%).

2.2. Photometry and Astrometry Cross Calibration

Following the same recipe as in Section 2.1.1, we check the accuracy of the HELM pipeline photometry and astrometry independently for the fields that are not covered by the official

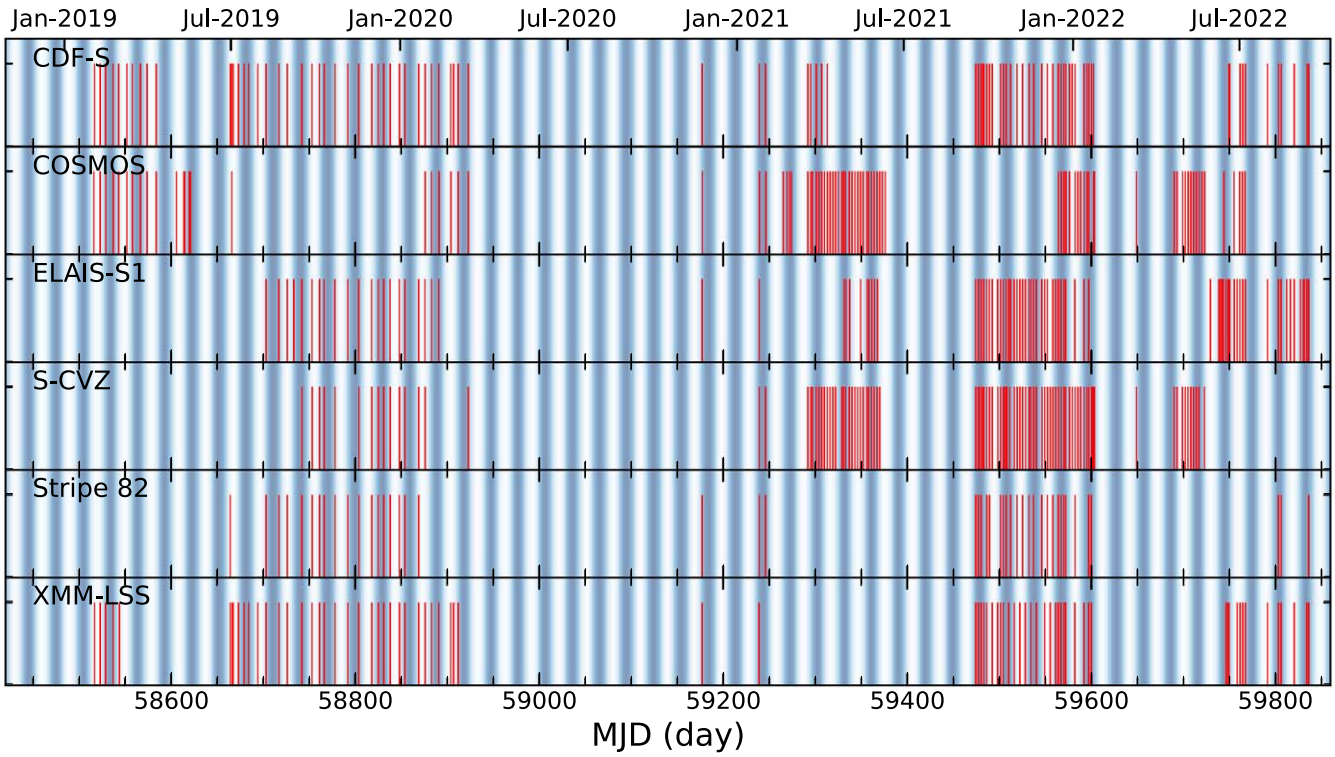

Figure 2. Cadence of the HELM in different fields, with vertical red lines indicating individual exposures. Moon illumination (illuminated fraction of the moon) is indicated by the blue gradient (white = no moonlight; dark blue = maximum moonlight) in the background.

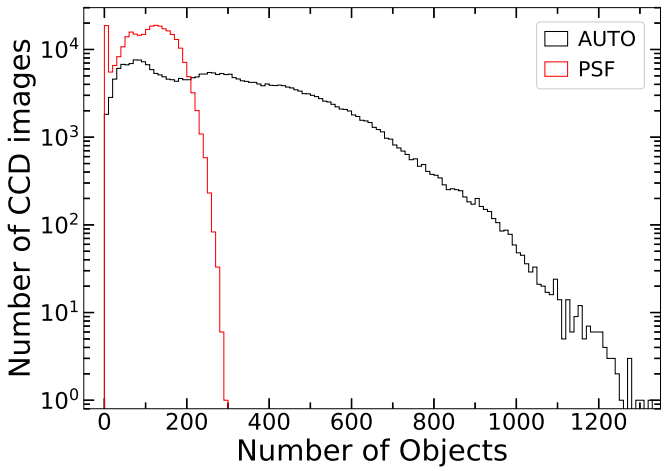

Figure 3. Histograms of objects used to calibrate the magnitude zero-point (zp) for each CCD image of every exposure. The histogram for point sources using $m_{\rm PSF}$ is in red (PSF), while the histogram for all sources using $m_{\rm AUTO}$ is in black.

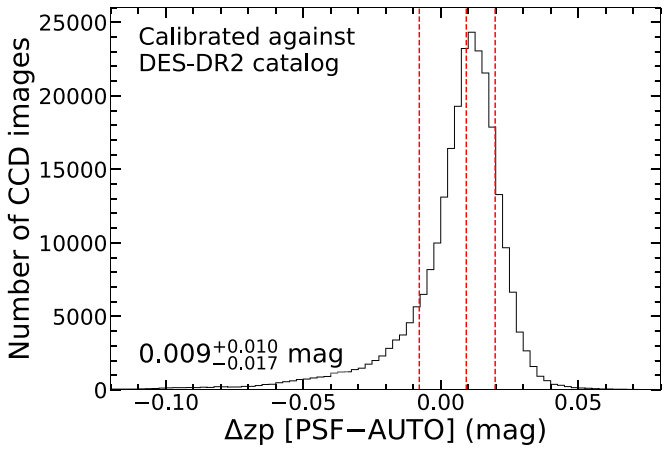

Figure 4. Comparison of magnitude zps calibrated against the DES-DR2 catalog using point sources (PSF) and all sources (AUTO). Only CCD images with at least 10 sources used for calibration are included. Red vertical dashed lines indicate the 16th, 50th, and 84th percentiles of the distribution, with statistics shown in the lower-left corner.

DES data products (COSMOS and S-CVZ). The DES-DR2 catalog is based on coadded images, with a photometric accuracy of ∼0.01 mag and astrometric precision of ∼0.″03. We select all the point sources detected in our observations and crossmatch with the DES-DR2 catalog for all the reliably extracted (`IMAFLAGS_ISO=0`, `FLAGS` <4), high-SNR ($m_{\rm PSF}$ error <0.1 mag) sources. We select point sources from the DES-DR2 catalog using $0 \leqslant$ `EXTENDED_COADD` $\leqslant 1$. For our observations, we use a relatively loose criterion of `CLASS_STAR` >0.8, which ensures we do not miss a significant number of point sources and avoids including many extended sources.

Figure 5 presents an example of comparison of $m_{\rm PSF}$ and coordinate difference (Δd) as a function of $m_{\rm PSF}$ error in pointing C1. The statistics for all 10 pointings are presented in Table 3. Although various degrees of differences are found in different fields, the source magnitude (median $\Delta m_{\rm PSF} \approx$ 0.02 mag) and astrometry ($\Delta d \approx 0.''06$) of our HELM pipeline are in good agreement with DES-DR2 for high-SNR sources. The overall good performances in zps, photometry, and astrometry lend support to the reliability of the HELM pipeline for use in fields not covered by the footprint of DES-DR2 (COSMOS and S-CVZ).

Table 2
Comparison of HELM zp, $m_{\rm PSF}$, and Astrometry to Those from DES-DR2

Pointing Field	Δzp (mag)	$\Delta m_{\rm PSF}$ (g) (mag)	$\Delta m_{\rm PSF}$ (r) (mag)	$\Delta m_{\rm PSF}$ (i) (mag)	$\Delta m_{\rm PSF}$ (z) (mag)	Δd (g) (arcsec)	Δd (r) (arcsec)	Δd (i) (arcsec)	Δd (z) (arcsec)
C1	$-0.007^{+0.017}_{-0.032}$	$-0.019^{+0.038}_{-0.042}$	$-0.026^{+0.036}_{-0.042}$	$-0.011^{+0.026}_{-0.029}$	$-0.015^{+0.024}_{-0.029}$	$0.059^{+0.054}_{-0.032}$	$0.052^{+0.050}_{-0.028}$	$0.050^{+0.047}_{-0.027}$	$0.050^{+0.045}_{-0.027}$
C2	$-0.006^{+0.015}_{-0.024}$	$-0.015^{+0.035}_{-0.036}$	$-0.020^{+0.034}_{-0.039}$	$-0.013^{+0.031}_{-0.028}$	$-0.015^{+0.028}_{-0.028}$	$0.059^{+0.054}_{-0.031}$	$0.052^{+0.050}_{-0.028}$	$0.051^{+0.047}_{-0.027}$	$0.051^{+0.046}_{-0.027}$
C3	$-0.005^{+0.018}_{-0.031}$	$-0.016^{+0.036}_{-0.041}$	$-0.018^{+0.032}_{-0.041}$	$-0.012^{+0.028}_{-0.030}$	$-0.018^{+0.025}_{-0.030}$	$0.066^{+0.063}_{-0.036}$	$0.060^{+0.060}_{-0.033}$	$0.058^{+0.057}_{-0.032}$	$0.052^{+0.048}_{-0.028}$
E1	$0.004^{+0.029}_{-0.043}$	$-0.029^{+0.037}_{-0.042}$	$0.020^{+0.039}_{-0.042}$	$0.007^{+0.032}_{-0.033}$	$-0.004^{+0.028}_{-0.028}$	$0.075^{+0.072}_{-0.040}$	$0.068^{+0.066}_{-0.036}$	$0.065^{+0.061}_{-0.035}$	$0.053^{+0.048}_{-0.028}$
E2	$-0.014^{+0.024}_{-0.035}$	$-0.037^{+0.036}_{-0.039}$	$-0.005^{+0.040}_{-0.034}$	$-0.014^{+0.032}_{-0.034}$	$-0.011^{+0.026}_{-0.025}$	$0.073^{+0.069}_{-0.039}$	$0.067^{+0.065}_{-0.036}$	$0.064^{+0.061}_{-0.034}$	$0.054^{+0.048}_{-0.029}$
S1	$-0.008^{+0.044}_{-0.029}$	$-0.023^{+0.045}_{-0.041}$	$-0.009^{+0.047}_{-0.032}$	$0.028^{+0.051}_{-0.043}$	$0.009^{+0.037}_{-0.026}$	$0.066^{+0.063}_{-0.036}$	$0.058^{+0.061}_{-0.032}$	$0.057^{+0.058}_{-0.031}$	$0.050^{+0.047}_{-0.027}$
S2	$0.000^{+0.026}_{-0.024}$	$0.009^{+0.052}_{-0.053}$	$-0.010^{+0.038}_{-0.033}$	$-0.009^{+0.032}_{-0.044}$	$-0.013^{+0.030}_{-0.037}$	$0.066^{+0.064}_{-0.036}$	$0.058^{+0.062}_{-0.032}$	$0.058^{+0.059}_{-0.032}$	$0.052^{+0.049}_{-0.028}$
X1	$-0.002^{+0.020}_{-0.035}$	$-0.008^{+0.041}_{-0.048}$	$-0.015^{+0.039}_{-0.045}$	$-0.008^{+0.031}_{-0.035}$	$-0.012^{+0.030}_{-0.034}$	$0.068^{+0.066}_{-0.036}$	$0.062^{+0.064}_{-0.034}$	$0.061^{+0.059}_{-0.033}$	$0.055^{+0.051}_{-0.030}$
X2	$0.004^{+0.019}_{-0.033}$	$-0.005^{+0.044}_{-0.051}$	$-0.008^{+0.041}_{-0.044}$	$-0.009^{+0.032}_{-0.037}$	$-0.015^{+0.029}_{-0.035}$	$0.070^{+0.068}_{-0.038}$	$0.064^{+0.064}_{-0.035}$	$0.062^{+0.061}_{-0.034}$	$0.056^{+0.051}_{-0.030}$
X3	$0.003^{+0.019}_{-0.030}$	$-0.009^{+0.042}_{-0.047}$	$-0.006^{+0.038}_{-0.041}$	$-0.003^{+0.031}_{-0.033}$	$-0.011^{+0.028}_{-0.029}$	$0.070^{+0.066}_{-0.038}$	$0.062^{+0.063}_{-0.034}$	$0.060^{+0.059}_{-0.033}$	$0.053^{+0.049}_{-0.028}$

Note. $\Delta \equiv$ our DECam data − DES-DR2. Statistics are 50th percentile with upper (84th−50th) and lower (16th−50th) 1σ of the distribution as the superscript and subscript, respectively. Δd represents the angular distance difference between coordinates.

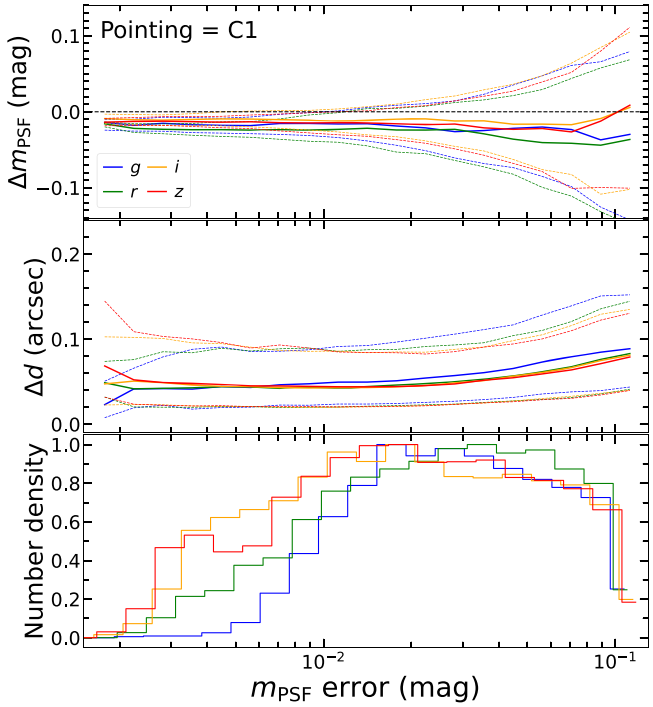

Figure 5. Differences in $m_{\rm PSF}$ (top) and coordinates (middle) between our measurements of all observations and those from the DES-DR2 catalog ($\Delta \equiv$ HELM − DES-DR2) as a function of $m_{\rm PSF}$ error for all high-SNR ($m_{\rm PSF}$ error <0.1 mag) point sources in pointing C1. Normalized source number density ($N/N_{\rm max}$) of the $m_{\rm PSF}$ error is shown in the bottom panel. $m_{\rm PSF}$ error is the propagated error by combining our measurement error and DES-DR2 measurement error in quadrature sum. Median values in the *griz* filters are shown as blue, green, orange, and red solid curves, respectively. Dashed curves in the top and middle panels indicate values at the 84th and 16th percentiles. Statistics of all 10 pointings are shown in Table 2.

3. Data Products

For this first HELM data release, we include the source catalog covering all compiled fields, as well as the light curves for these sources from the first 3.5 yr (2019A–2022A). Our source catalog is built by crossmatching reliably extracted (`IMAFLAGS_ISO=0`, `FLAGS` <4) sources in our individual images with the DES-DR2 (T. M. C. Abbott et al. 2021) source catalog for the CDF-S, XMM-LSS, ELAIS-S1, and SDSS Stripe 82 fields, and with the source catalog from the third data release (H. Aihara et al. 2022) of the Hyper Suprime-Cam (HSC) Subaru Strategic Program (SSP; H. Aihara et al. 2018) for the COSMOS field. In total, there are 5,404,721, 4,714,784, and 4,059,093 sources with detections in at least 3, 5, and 10 exposures in any band, respectively. Figure 6 shows histograms of inverse variance-weighted mean $m_{\rm AUTO}$ ($m_{\rm AUTO}$_w; see Section 3.1 for definition) in the *gri* bands for objects in all six fields with detections in at least five individual exposures. The peak $m_{\rm AUTO}$_w is ∼24.0, 23.6, and 23.4 mag for the *gri* bands, respectively, which are deeper compared to those of typical single exposures (Table 1) and represent the best seeing condition and longest exposure time. Using the the largest value of the `class_star_m` (median `class_star` of individual exposures in one band; see Table 3) in the *gri* bands to roughly classify objects as unresolved/barely resolved (⩾0.9) or resolved objects (<0.9), unresolved/barely resolved sources account for 7.2%, 21.0%, 6.9%, 40.1%, 11.6%, and 11.1% of the total sources in the CDF-S, COSMOS, ELAIS-S1, S-CVZ, Stripe 82, and XMM-LSS fields, respectively. The slightly higher fraction in the COSMOS field is likely due to the detection of more unresolved/barely resolved faint galaxies detected by HSC-SSP COSMOS observations, while the much higher stellar density is attributed to the significantly elevated fraction in the S-CVZ field. In future data releases, we will provide individual images, deeper photometric catalogs built from the coadded images, and extended light curves (see Section 4). Below we describe in detail our source catalog and light-curve compilation.

3.1. Source Catalogs and Light Curves

The majority of our DECam pointings in the COSMOS field are covered by Deep- and UltraDeep-depth images of HSC-SSP. For regions outside the Deep and UltraDeep coverage, we use instead the source catalog from Wide-depth images of HSC-SSP. We extract the source catalog with an *i*-band `Kron` magnitude brighter than 25.5 mag from the HSC Legacy Archive[49] (`pdr3_dud_rev` for the Deep and UltraDeep catalogs and `pdr3_wide` for the Wide catalog) using the example script `PDR3 example 1a`. For the Wide catalog, we further apply the criteria presented in the `PDR3 example 6` script to the *i* band to keep only "clean" sources. For all the

[49] https://hscla.mtk.nao.ac.jp/doc/

Table 3
FITS Table Format for the Median Source Catalog

Column Name	Format	Units	Description
Index	LONG		Source index
ra	DOUBLE	degrees	R.A. (J2000)
dec	DOUBLE	degrees	Decl. (J2000)
mag_psf	DOUBLE	mag	`SExtractor` PSF magnitude
mag_auto	DOUBLE	mag	`SExtractor` AUTO magnitude
flags	LONG		`SExtractor` extraction flags
spread_model	DOUBLE		`SExtractor` model-based star–galaxy classifier
class_star	DOUBLE		`SExtractor` neural network–based star–galaxy classifier
Nexp_psf	LONG		Number of exposures with successful mag_psf measurement
Nexp_auto	LONG		Number of exposures with successful mag_auto measurement
Separation	DOUBLE	arcsec	Distance between median coordinate in *griz* bands and *u* band (only in S-CVZ field)

Note. All columns except Separation can have a prefix, while all columns except Index, Nexp_psf, Nexp_auto, and Separation have a suffix. Prefix: "*_" indicates the associated band for the parameter, with * = 1 or a combination of *ugriz* bands (such as g_ in all fields or griz_only for S-CVZ). If not specified (for Index, ra, and dec in all fields except S-CVZ), it represents the value for all bands combined. Suffix: "_m" and "_err" indicate the unweighted median (50%) and its corresponding error of $N_{\rm exp}$ measurements with _err =0.5 × (84th percentile − 16th percentile)$/\sqrt{N_{\rm exp}}$; "_w" indicates the inverse variance-weighted mean ($\Sigma(m_i/e_i^2)/\Sigma(1/e_i^2)$, where m_i and e_i represent individual measurement and its error at ith exposure, respectively); "_w_err" indicates the error associated with _w after error propagation ($1/\sqrt{\Sigma(1/e_i^2)}$). Specifically, "_err" = "_w_err" = error of individual measurement when $N_{\rm exp} = 1$. Value = "−99" indicates no data or nondetection.

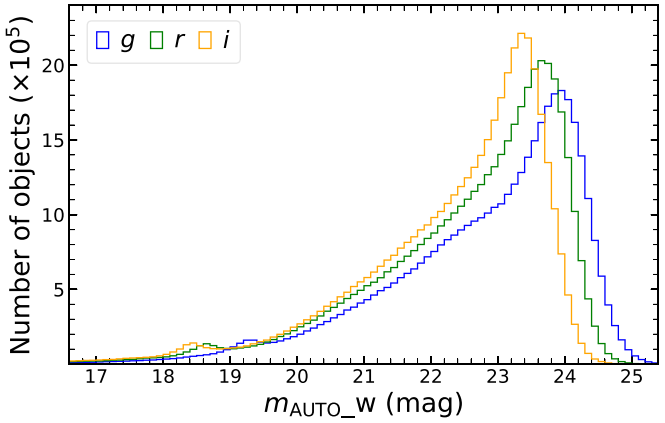

Figure 6. Histograms of inverse variance-weighted mean $m_{\rm AUTO}$ in all detected exposures ($m_{\rm AUTO}$_w; see Equation (1)) in *g* (blue), *r* (green), and *i* (orange) bands for objects in all six fields with detection in at least five individual exposures.

other fields except S-CVZ (i.e., CDF-S, ELAIS-S1, Stripe 82, and XMM-LSS), we use DES-DR2 as the base source catalog for catalog construction, as it is deeper than individual exposures of our program. A radius of 0.″5 is adopted for crossmatching.

For the S-CVZ field, we construct the source catalog from scratch as no deep optical catalog in this field is currently available. We first randomly pick an individual exposure catalog as the reference catalog and crossmatch other catalogs in the *griz* bands to it one by one using a matching radius of 0.″5. We then iteratively build the preliminary master catalog by adding new sources whose separations from existing sources are larger than 0.″5. The coordinates of the preliminary master catalog obtained after the first run are determined as the median value of those classified as the same source in individual catalogs. We then perform a second run by crossmatching individual exposure catalogs to the preliminary master catalog and obtain a final catalog in the *griz* bands. Finally, we crossmatch the *u*-band individual exposure catalogs with the *griz* catalog, as the *u*-band depth is much shallower compared to that in the *griz* bands.

Table 4
FITS Table Format for the Light Curve

Column Name	Format	Units	Description
ra	DOUBLE	degrees	R.A. (J2000)
dec	DOUBLE	degrees	Decl. (J2000)
expnum	LONG		DECam exposure number
mjd	DOUBLE	days	Modified Julian date of exposure
band	Char		Filter (one of *ugriz*)
mag_psf	DOUBLE	mag	`SExtractor` PSF magnitude
mag_e_psf	DOUBLE	mag	Uncertainty of `SExtractor` PSF magnitude
mag_auto	DOUBLE	mag	`SExtractor` AUTO magnitude
mag_e_auto	DOUBLE	mag	Uncertainty of `SExtractor` AUTO magnitude
flags	LONG		`SExtractor` extraction flags
spread_model	DOUBLE		`SExtractor` model-based star–galaxy separation
spread_model_e	DOUBLE		Uncertainty of `SExtractor` model-based star–galaxy separation
class_star	DOUBLE		`SExtractor` neural network–based star–galaxy separation

Our median source catalog and light curves include both persistent and variable sources. Table 3 presents the table format of our median source catalog, including source index, coordinate, magnitudes (PSF and AUTO), extraction flags, star–galaxy classifier (spread_model and class_star), and number of exposures. For magnitude, we also provide inverse variance-weighted mean (mag_w), defined as

$$\text{mag\_w} \equiv \frac{\Sigma(m_i/e_i^2)}{\Sigma(1/e_i^2)}, \tag{1}$$

where m_i and e_i represent an individual measurement and its error in the ith exposure, respectively. Its corresponding uncertainty is

$$\text{mag\_w\_err} = \frac{\sqrt{\Sigma(e_i/e_i^2)^2}}{\Sigma(1/e_i^2)} = \frac{1}{\sqrt{\Sigma(1/e_i^2)}}, \tag{2}$$

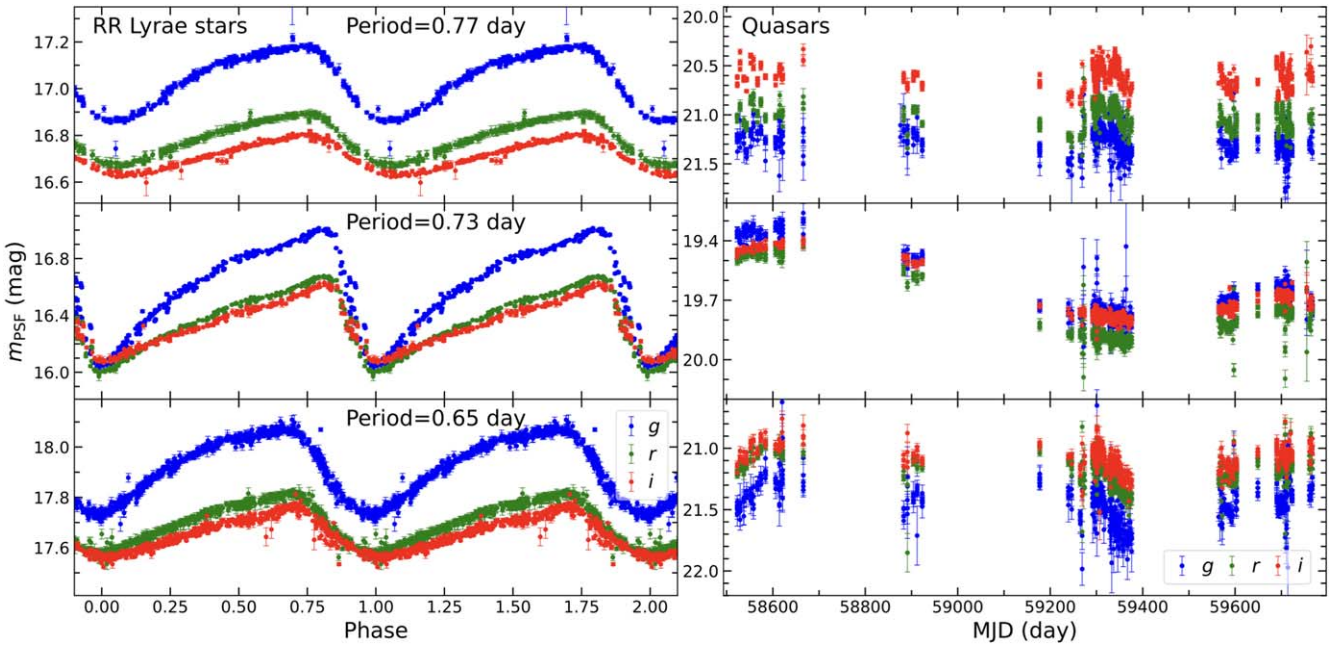

Figure 7. Example light curves of RR Lyrae stars (left; in folded phase) and AGNs (right) in the COSMOS field. Blue, green, and red dots represent the *g*, *r*, and *i* bands, respectively, with error bars indicating the certainty. The periods of RR Lyrae stars are shown at the top of the left panels.

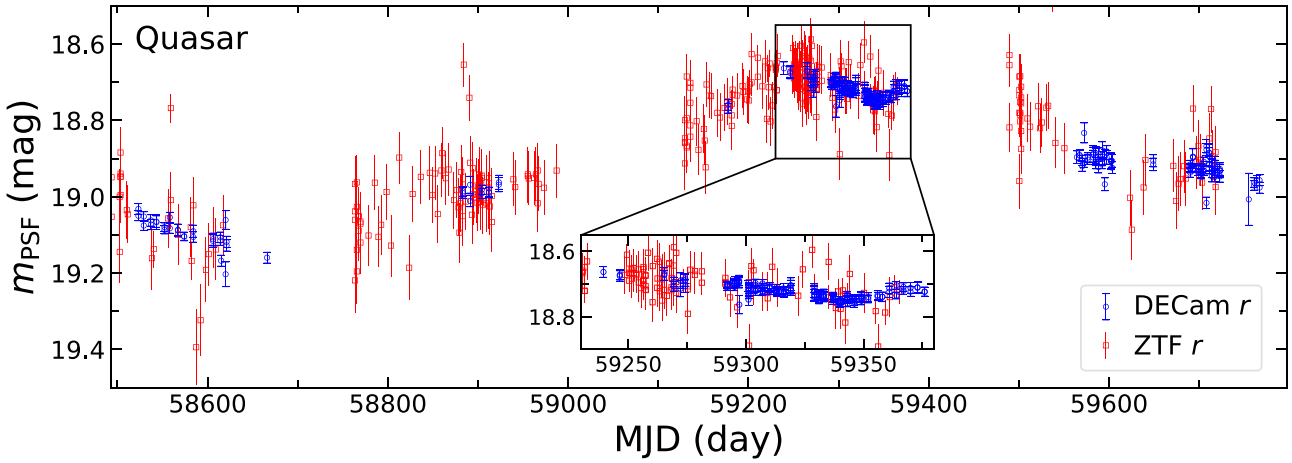

Figure 8. Comparison of DECam *r*-band (open blue circle) and ZTF *r*-band (open red square) light curves of a quasar in the COSMOS field. The inset shows a zoomed-in view around MJD = 59300 days. The error bars indicate 1σ uncertainty.

after error propagation. For the S-CVZ field, we provide separate source indices and coordinates for the *griz* and *u* bands, as the *u* band is much shallower compared to the other bands. Separation between the median coordinate in the *griz* bands and that in the *u* band is also provided. Table 4 describes the format of the light-curve files of individual objects. The light curves of individual sources can be extracted from our online database[50] using source indices provided in Table 3.

3.2. Example Light Curves

Figure 7 shows example light curves of three RR Lyrae stars and three quasars in the COSMOS field. For RR Lyrae stars, we have modeled their light curves using `astropy` and presented phase-folded light curves. The high-quality photometry and dense time sampling ensure excellent recovery of period information. The overall clean phase-folded light curves of RR Lyrae stars also demonstrate the good performance of our zp calibration (Section 2.2). The long time baseline, decent ∼3 day cadence, and multiband coverage make it possible to qualitatively investigate both long and short timescales, as well as multiband AGN variability. In particular, as shown in Figure 8 and its inset, the epoch magnitude uncertainty is ∼5 times smaller in HELM than in the ZTF DR19—median uncertainty of 0.014 mag from the HELM *r* band versus 0.068 mag from the ZTF *r* band. Therefore the resulting optical light curves from HELM are of much better quality than the ZTF light curves, albeit with sparser cadences.

3.3. Caveats

In this paper, our source catalogs for the CDF-S, ELAIS-S1, Stripe 82, and XMM-LSS fields are constructed based on the DES-DR2 source catalog, which has a median coadded catalog depth for a $1\farcs95$ diameter aperture at SNR = 10 of $g = 24.7$,

[50] https://ariel.astro.illinois.edu/helm/

$r = 24.4$, $i = 23.8$, and $z = 23.1$ mag. However, we may miss transients that were not detected (did not have optical counterparts) in previous surveys. Given the number of exposures (up to 387 s) and total exposure time (up to 4480 s) in these fields, together with ongoing exposures that are not included in this data release, we would eventually achieve much deeper source detection by coadding all individual exposures. For the S-CVZ field, our source catalog is constructed based on catalogs of individual exposures. Therefore, the depth is limited by the deepest exposure. For the COSMOS field, we notice a source-splitting issue for saturated objects in the HSC catalog. As we are using deeper catalogs for source crossmatching (in particular for the COSMOS field), our source catalog may contain some spurious sources with low $N_{\rm exp}$ and close to or even below the typical depth of DECam individual exposures (a relatively steep increase of source number toward the faint end in the *g* and *i* bands as seen in Figure 6). Moreover, as the saturation magnitudes are quite faint for the HSC survey (18.0, 18.2, and 18.6 mag for the *gri* bands; H. Aihara et al. 2018), this issue may affect the sources that are above their saturation limits. Another major caveat is that there is no forced photometry or upper limits for each epoch in the light curves. This is because the catalog of individual exposure is constructed independently and the detection (or not) of a faint source in a specific exposure (epoch) depends critically on the detection limit of that exposure. This may give a false sense of the overall variability especially for sources close to the detection limit. The caveats mentioned above would be largely mitigated by building source catalogs directly from coadded DECam images and performing forced photometry on each source in our future data releases. On the other hand, any variable/transient sources that are not associated with a static object in the matched catalogs will be missed (e.g., off-axis transients and moving objects). These objects will be included in our future data releases after implementing a dedicated pipeline.

4. Summary

In this work we present an overview of the HELM long-term monitoring program in extragalactic legacy fields, with the DECam imager on the 4 m CTIO Blanco telescope. With a multiyear baseline and relatively high cadence, HELM aims to provide high-quality optical light curves for a large sample of AGNs in these fields, as part of the effort to obtain RM measurements for distant AGNs and quasars in the SDSS-V BHM-RM program. This long-term photometric monitoring program will also bridge past light curves and future LSST/WFST observations to compile decades-long light curves to facilitate investigations of long-term variability of astronomical objects (particularly AGNs). Given the ample multiwavelength data in these legacy fields, the HELM light-curve data will also provide legacy value to time-domain studies. At the time of writing, HELM has been extended to continue DECam monitoring in these fields through at least 2025B, given the delayed start of the LSST.

In this work we also present the first data release from HELM, which includes source catalogs and light curves from the first 3.5 yr of observations. In future data releases, we will provide fully calibrated individual and coadded images, as well as extended light curves.

Acknowledgments

We thank Tamara M. Davis for initial discussions. This work is supported by NSF grants AST-2206499 and AST-2308077. R.J.A. was supported by FONDECYT grant No. 1231718 and by the ANID BASAL project FB210003. F.E.B. acknowledges support from ANID—Millennium Science Initiative Program—ICN12_009, CATA-BASAL—FB210003, and FONDECYT Regular—1200495. Y.Q.X. acknowledges support from the National Key R&D Program of China (2023YFA1608100), NSFC grants (12025303, 12393814), and the Strategic Priority Research Program of the Chinese Academy of Sciences (XDB0550300).

Since 2021, this DECam program is a founding member of the DECam Alliance for Transients (DECAT), a logistical solution for a heterogenous group of programs all doing time-domain astronomy on a classically scheduled telescope. Within DECAT, multiple DECam programs request that their awarded time be coscheduled on the Blanco 4 m telescope, and then the PIs work together to ensure the targets for all programs are optimally observed, and all program participants share in the observing responsibilities. We thank all NOIRLab and Blanco staff for their flexibility and support in helping to coschedule all DECAT programs. The DECAT nightly observing plans were primarily generated by Gautham Narayan, Dillon Brout, and Armin Rest.

This project used data obtained with the Dark Energy Camera (DECam), which was constructed by the Dark Energy Survey (DES) collaboration. Funding for the DES Projects has been provided by the U.S. Department of Energy, the U.S. National Science Foundation, the Ministry of Science and Education of Spain, the Science and Technology Facilities Council of the United Kingdom, the Higher Education Funding Council for England, the National Center for Supercomputing Applications at the University of Illinois at Urbana-Champaign, the Kavli Institute of Cosmological Physics at the University of Chicago, Center for Cosmology and Astro-Particle Physics at the Ohio State University, the Mitchell Institute for Fundamental Physics and Astronomy at Texas A&M University, Financiadora de Estudos e Projetos, Fundacao Carlos Chagas Filho de Amparo, Financiadora de Estudos e Projetos, Fundacao Carlos Chagas Filho de Amparo a Pesquisa do Estado do Rio de Janeiro, Conselho Nacional de Desenvolvimento Cientifico e Tecnologico and the Ministerio da Ciencia, Tecnologia e Inovacao, the Deutsche Forschungsgemeinschaft, and the Collaborating Institutions in the Dark Energy Survey. The collaborating institutions are Argonne National Laboratory, the University of California at Santa Cruz, the University of Cambridge, Centro de Investigaciones Energeticas, Medioambientales y Tecnologicas-Madrid, the University of Chicago, University College London, the DES-Brazil Consortium, the University of Edinburgh, the Eidgenossische Technische Hochschule (ETH) Zurich, Fermi National Accelerator Laboratory, the University of Illinois at Urbana-Champaign, the Institut de Ciencies de l'Espai (IEEC/CSIC), the Institut de Fisica d'Altes Energies, Lawrence Berkeley National Laboratory, the Ludwig Maximilians Universitat Munchen and the associated Excellence Cluster Universe, the University of Michigan, NSF's NOIRLab, the University of Nottingham, the Ohio State University, the University of Pennsylvania, the University of Portsmouth, SLAC National Accelerator Laboratory, Stanford University, the University of Sussex, and Texas A&M University.

Facility: Blanco

Software: `astropy` (Astropy Collaboration et al. 2013, 2018), `Matplotlib` (J. D. Hunter 2007), `Numpy` (C. R. Harris et al. 2020),

ORCID iDs

Ming-Yang Zhuang (庄明阳) https://orcid.org/0000-0001-5105-2837
Qian Yang https://orcid.org/0000-0002-6893-3742
Yue Shen https://orcid.org/0000-0003-1659-7035
Monika Adamów https://orcid.org/0000-0002-6904-359X
Douglas N. Friedel https://orcid.org/0000-0002-3632-7668
R. A. Gruendl https://orcid.org/0000-0002-4588-6517
Zachary Stone https://orcid.org/0000-0002-8501-3518
Junyao Li https://orcid.org/0000-0002-1605-915X
Xin Liu https://orcid.org/0000-0003-0049-5210
Paul Martini https://orcid.org/0000-0002-4279-4182
Timothy M. C. Abbott https://orcid.org/0000-0003-1587-3931
Scott F. Anderson https://orcid.org/0000-0002-6404-9562
Roberto J. Assef https://orcid.org/0000-0002-9508-3667
Franz E. Bauer https://orcid.org/0000-0002-8686-8737
Richard Bielby https://orcid.org/0000-0001-9070-9969
W. N. Brandt https://orcid.org/0000-0002-0167-2453
Colin J. Burke https://orcid.org/0000-0001-9947-6911
Jorge Casares https://orcid.org/0000-0001-5031-0128
Yu-Ching Chen https://orcid.org/0000-0002-9932-1298
Gisella De Rosa https://orcid.org/0000-0003-3242-7052
Alex Drlica-Wagner https://orcid.org/0000-0001-8251-933X
Tom Dwelly https://orcid.org/0000-0002-4459-9233
Gloria Fonseca Alvarez https://orcid.org/0000-0003-0042-6936
Jianyang Fu (傅健洋) https://orcid.org/0000-0002-3767-299X
Cesar Fuentes https://orcid.org/0000-0002-5211-0020
Melissa L. Graham https://orcid.org/0000-0002-9154-3136
Catherine J. Grier https://orcid.org/0000-0001-9920-6057
Nathan Golovich https://orcid.org/0000-0003-2632-572X
Patrick B. Hall https://orcid.org/0000-0002-1763-5825
Patrick Hartigan https://orcid.org/0000-0002-5380-549X
Keith Horne https://orcid.org/0000-0003-1728-0304
Anton M. Koekemoer https://orcid.org/0000-0002-6610-2048
Jennifer I. Li https://orcid.org/0000-0002-0311-2812
Chris Lidman https://orcid.org/0000-0003-1731-0497
Umang Malik https://orcid.org/0000-0002-0036-1696
Amelia Mangian https://orcid.org/0000-0003-2385-6904
Andrea Merloni https://orcid.org/0000-0002-0761-0130
Claudio Ricci https://orcid.org/0000-0001-5231-2645
Mara Salvato https://orcid.org/0000-0001-7116-9303
Rob Sharp https://orcid.org/0000-0003-4877-7866
David E. Trilling https://orcid.org/0000-0003-4580-3790
Brad E. Tucker https://orcid.org/0000-0002-4283-5159
Di Wen https://orcid.org/0000-0003-2812-8607
Zachary Wideman https://orcid.org/0000-0001-8171-5507
Yongquan Xue https://orcid.org/0000-0002-1935-8104
Zhefu Yu https://orcid.org/0000-0003-0644-9282
Catherine Zucker https://orcid.org/0000-0002-2250-730X

References

Abbott, T. M. C., Adamów, M., Aguena, M., et al. 2021, ApJS, 255, 20
Aihara, H., AlSayyad, Y., Ando, M., et al. 2022, PASJ, 74, 247
Aihara, H., Arimoto, N., Armstrong, R., et al. 2018, PASJ, 70, S4
Astropy Collaboration, Price-Whelan, A. M., Sipőcz, B. M., et al. 2018, AJ, 156, 123
Astropy Collaboration, Robitaille, T. P., Tollerud, E. J., et al. 2013, A&A, 558, A33
Bellm, E. C., Kulkarni, S. R., Graham, M. J., et al. 2019, PASP, 131, 018002
Bernstein, J. P., Kessler, R., Kuhlmann, S., et al. 2012, ApJ, 753, 152
Bertin, E. 2011, in ASP Conf. Ser. 442, Astronomical Data Analysis Software and Systems XX, ed. I. N. Evans (San Francisco, CA: ASP), 435
Bertin, E., & Arnouts, S. 1996, A&AS, 117, 393
Blandford, R. D., & McKee, C. F. 1982, ApJ, 255, 419
Chambers, K. C., Magnier, E. A., Metcalfe, N., et al. 2016, arXiv:1612.05560
Drlica-Wagner, A., Ferguson, P. S., Adamów, M., et al. 2022, ApJS, 261, 38
Flaugher, B., Diehl, H. T., Honscheid, K., et al. 2015, AJ, 150, 150
Graham, M. J., Djorgovski, S. G., Stern, D., et al. 2015, MNRAS, 453, 1562
Graham, M. L., Knop, R. A., Kennedy, T. D., et al. 2023, MNRAS, 519, 3881
Harris, C. R., Millman, K. J., van der Walt, S. J., et al. 2020, Natur, 585, 357
Henden, A. A., Levine, S., Terrell, D., & Welch, D. L. 2015, AAS Meeting, 225, 336.16
Hunter, J. D. 2007, CSE, 9, 90
Jones, D. O., Scolnic, D. M., Riess, A. G., et al. 2017, ApJ, 843, 6
Kollmeier, J. A., Zasowski, G., Rix, H.-W., et al. 2017, arXiv:1711.03234
Lacy, M., Surace, J. A., Farrah, D., et al. 2021, MNRAS, 501, 892
Morganson, E., Gruendl, R. A., Menanteau, F., et al. 2018, PASP, 130, 074501
Peterson, B. M. 1993, PASP, 105, 247
Sako, M., Bassett, B., Becker, A. C., et al. 2018, PASP, 130, 064002
Shen, Y., Brandt, W. N., Dawson, K. S., et al. 2015, ApJS, 216, 4
Smith, M., D'Andrea, C. B., Sullivan, M., et al. 2020, AJ, 160, 267
Wang, T., Liu, G., Cai, Z., et al. 2023, SCPMA, 66, 109512
York, D. G., Adelman, J., & Anderson, J. E. J. 2000, AJ, 120, 1579
Zou, F., Brandt, W. N., Chen, C.-T., et al. 2022, ApJS, 262, 15